



He, A., Li, H.-T., Lan, X., Liang, Y. and Zhao, O. (2020) Flexural buckling behaviour and residual strengths of stainless steel CHS columns after exposure to fire. *Thin-Walled Structures*, 152, 106715. (doi: [10.1016/j.tws.2020.106715](https://doi.org/10.1016/j.tws.2020.106715))

There may be differences between this version and the published version. You are advised to consult the publisher's version if you wish to cite from it.

<http://eprints.gla.ac.uk/223677/>

Deposited on 8 March 2021

Enlighten – Research publications by members of the University of Glasgow  
<http://eprints.gla.ac.uk>

# 1 **Flexural buckling behaviour and residual strengths of stainless steel CHS** 2 **columns after exposure to fire**

3 An He <sup>a</sup>, Hai-Ting Li <sup>b</sup>, Xiaoyi Lan <sup>c</sup>, Yating Liang <sup>d</sup>, Ou Zhao <sup>\*e</sup>

4 <sup>a, b, c, e</sup> School of Civil and Environmental Engineering, Nanyang Technological University, Singapore

5 <sup>d</sup> School of Engineering, University of Glasgow, Glasgow, UK

6  
7 \* Corresponding author, Email: ou.zhao@ntu.edu.sg

## 8 9 10 **Abstract**

11  
12 The flexural buckling behaviour and residual strengths of stainless steel circular hollow section  
13 (CHS) columns after exposure to fire were studied, based on a thorough experimental and  
14 numerical modelling programme, and reported in this paper. The experimental programme was  
15 performed on three series of specimens, and each series contained five geometrically identical  
16 specimens, with one unheated and the other four heated to different levels of elevated  
17 temperatures (namely 300 °C, 600 °C, 800 °C and 1000 °C). The detailed heating, soaking and  
18 cooling processes, material testing and pin-ended column tests were described, with the derived  
19 key experimental results fully presented. The testing programme was supplemented by a  
20 numerical modelling programme, including a validation study where finite element models  
21 were developed and validated against the test results, and a parametric study where the  
22 validated finite element models were employed to derive further numerical results over an  
23 extended range of cross-section dimensions and member lengths. Due to the absence of existing  
24 design codes for stainless steel structures after exposure to fire, the codified design provisions  
25 for stainless steel CHS columns at ambient temperature, as established in the Europe, America

26 and Australia/New Zealand, were assessed for their applicability to stainless steel CHS  
27 columns after exposure to fire, based on the obtained test and numerical data. The assessment  
28 results generally revealed that the design buckling curve, as adopted in the European code, and  
29 the tangent modulus method, as employed in the American specification, lead to unsafe and  
30 scattered design flexural buckling strengths for stainless steel CHS columns after exposure to  
31 fire, while the explicit approach, as used in the Australian/New Zealand standard, yields a high  
32 level of accuracy and consistency in predicting the post-fire flexural buckling strengths of  
33 stainless steel CHS columns.

34

35 **Keywords:** Circular hollow section (CHS); Design analysis; Flexural buckling behaviour;  
36 Heating, soaking and cooling processes; Material tensile coupon tests; Numerical modelling;  
37 Pin-ended column tests; Post-fire residual strengths; Stainless steel

38

39

## 40 **1. Introduction**

41

42 Stainless steel circular hollow sections (CHS) have been increasingly used in civil and offshore  
43 engineering, as they uniquely combine the material advantages of stainless steel, including high  
44 strength, superior ductility and excellent durability, with the favourable geometric  
45 characteristics of circular profiles, including the same cross-section properties in all directions,  
46 high torsional stiffness and low drag coefficient. Moreover, stainless steel CHS structural  
47 members not only grab the attention of architects and designers, but also attract the interests of  
48 researchers, with a brief summary of their previous experimental, numerical and analytical  
49 studies provided herein. At cross-sectional level, the local buckling behaviour and compression  
50 capacities of stainless steel CHS stub columns were investigated, based on extensive testing

51 programmes [1-9], while the in-plane flexural behaviour and capacities of stainless steel CHS  
52 beams were examined through a series of tests [2, 10-12], all indicating that the current design  
53 codes yield overly conservative and scattered predictions of cross-section compression and  
54 bending moment capacities, due to the use of the 0.2% proof stress as the failure stress in the  
55 design without accounting for the pronounced material strain hardening of stainless steel. Zhao  
56 et al. [13, 14] experimentally and numerically investigated the local stability and capacities of  
57 stainless steel CHS stub columns under combined compression and bending moment, and  
58 pointed out the conservatism of the codified cross-section interaction formulations, of which  
59 the major shortcoming lies in the neglect of the pronounced material strain hardening effect in  
60 the design. Improved design approaches for stainless steel CHS structural components prone  
61 to local buckling were then developed by Zhao et al. [14] and Buchanan et al. [15] based on  
62 the continuous strength method (CSM) [16-20], and the new proposals account for strain  
63 hardening in the predictions of cross-section capacities under both isolated and combined  
64 loadings and result in substantially higher levels of design accuracy and consistency than the  
65 established codes. At member level, experimental investigations into the flexural buckling  
66 behaviour and strengths of stainless steel CHS long columns were carried out and reported in  
67 Buchanan et al. [21], where the codified design buckling curves were found to yield inaccurate  
68 predictions of flexural buckling strengths and new design buckling curves were also proposed  
69 and validated against the experimental data, indicating a higher degree of design accuracy.  
70 Zhao et al. [22] and Buchanan et al. [23] conducted thorough experimental and numerical  
71 studies of stainless steel CHS long beam-columns, examined their global stability and strengths  
72 under combined compression and bending moment, assessed the accuracy of the codified  
73 design interaction expressions and finally devised more accurate and efficient design proposals.  
74 It is worth noting that the aforementioned previous research efforts focused on the behaviour  
75 and capacities of stainless steel CHS structural components at ambient temperature; however,

76 to date, their structural performance and residual strengths in fire and after exposure to fire  
77 remain unexplored. A research project has thus been initiated by the authors, aimed at  
78 investigating the fire and post-fire performances of various types of stainless steel CHS  
79 structural components. The material properties, local buckling behaviour and residual  
80 capacities of stainless steel CHS stub columns after exposed to fire has been examined and  
81 reported in He et al. [24], while the post-fire flexural buckling behaviour and strengths of  
82 stainless steel CHS long columns were investigated in the present study.

83

84 In the current work, a testing programme was firstly carried out on three series of stainless steel  
85 CHS column specimens, with each series containing five geometrically identical specimens,  
86 including one unheated specimen and four specimens heated to different levels of elevated  
87 temperatures. A numerical modelling programme was then performed, where finite element  
88 models were initially developed to simulate the test post-fire flexural buckling responses and  
89 then employed to conduct parametric studies to derive further numerical data over an extended  
90 range of cross-section sizes and member lengths. Given that there have been no existing design  
91 standards for stainless steel structures after exposure to fire, the flexural buckling design rules  
92 for stainless steel CHS columns at ambient temperature, as specified in EN 1993-1-4 [25],  
93 SEI/ASCE-8 [26] and AS/NZS 4673 [27], were evaluated for their applicability to stainless  
94 steel CHS columns after exposure to fire, based on the experimental and numerical data.

95

96

97

98

99

100

## 101 **2. Experimental study**

102

### 103 **2.1 General**

104

105 Two circular hollow sections CHS 73×3 and CHS 89×3, cold-rolled and seam-welded from  
106 grade EN 1.4301 austenitic stainless steel sheets, were adopted in the testing programme. The  
107 cross-section designation system consists of the letters ‘CHS’ (indicating a circular hollow  
108 section) and the nominal section size in millimetres (outer cross-section diameter  $D$  × wall  
109 thickness  $t$ ). Both of the two cross-sections at ambient temperature are categorised as Class 1  
110 according to the slenderness limits specific in EN 1993-1-4 [25]. Two nominal member lengths  
111 respectively equal to six and nine times the nominal outer cross-section diameter were  
112 employed for the CHS 73×3 column specimens, leading to two specimen series D73-L6 and  
113 D73-L9; the designation system of the specimen series starts with a letter ‘D’ (representing  
114 diameter) and the nominal outer cross-section diameter in millimetre (i.e. 73), followed by a  
115 letter ‘L’ (signifying length), and ends with a number ‘6’ or ‘9’ (i.e. the ratio of the nominal  
116 member length to the nominal outer cross-section diameter), while the nominal lengths of the  
117 CHS 89×3 column specimens were all equal to six times the nominal outer cross-section  
118 diameter, with the resulting specimen series denoted as D89-L6. Each of the three specimen  
119 series includes five geometrically identical column specimens, with one unheated and the other  
120 four heated to various levels of elevated temperatures (with the target values of 300 °C, 600 °C,  
121 800 °C and 1000 °C, respectively). The identifier of each specimen contains the specimen series,  
122 a letter ‘T’ (representing temperature) and the target elevated temperature, e.g., D89-L6-T800  
123 represents a CHS 89×3 column specimen with the nominal member length equal to six times  
124 the nominal outer cross-section diameter and the target heating temperature of 800 °C. Table 1  
125 summarises the target heating temperature  $T_n$  and the measured geometric dimensions of each

126 column specimen. In the following Section 2.2, the detailed heating, soaking and cooling  
127 processes were described, while the material tensile coupons tests, initial geometric  
128 imperfection measurements and pin-ended column tests were respectively reported in Sections  
129 2.3–2.5.

130

## 131 ***2.2 Heating, soaking and cooling processes***

132

133 A Nabertherm forced convection furnace was used to heat the specimens. The chamber of the  
134 furnace, as shown in Fig. 1, contains a series of embedded heating elements distributed  
135 uniformly over the four sides, and is also equipped with a fan and air baffles to allow for air  
136 circulation during heating, thus ensuring a high degree of temperature uniformity within the  
137 chamber. The columns specimens, together with the coupon specimens cut from the stainless  
138 steel CHS tubes, were placed on the bottom air baffle and just in front of the fan (where the  
139 optimum air circulation during heating was achieved), and then heated from the ambient  
140 temperature to each pre-specified level of elevated temperature at a rate of 10 °C/min, which is  
141 similar to the temperature increase rate of protected steelwork in fire. Upon attainment of the  
142 target temperature, it was maintained for half an hour (i.e. the soaking time of 30 mins), to  
143 ensure that the surface temperatures of the specimens were stable and uniform. When the  
144 soaking period was completed, the furnace was switched off, and the column and coupon  
145 specimens were naturally cooled down to the ambient temperature. During the heating, soaking  
146 and cooling processes, the actual surface temperatures of each group of column and coupon  
147 specimens (i.e. the specimens heated together to the same target elevated temperature) were  
148 measured through two thermocouples attached to the outer and inner surfaces of a  
149 representative column specimen, as depicted in Fig. 1. The temperatures measured at the inner  
150 and outer surfaces of each representative column specimen were almost the same during the

151 whole heating, soaking and cooling processes; the temperature–time curves, recorded by the  
152 two thermocouples, for a typical group of specimens exposed to a target level of elevated  
153 temperature equal to 600 °C are depicted in Fig. 2. The measured maximum surface  
154 temperature  $T$  for each group of specimens, taken as the average reading from the  
155 thermocouples during the soaking period, is presented in Table 1. Grade EN 1.4301 austenitic  
156 stainless steel displayed obvious changes in surface colour after exposure to elevated  
157 temperatures [24]. As exhibited in Fig. 3, the surface colours of grade EN 1.4301 austenitic  
158 stainless steel turned into bright yellow, dark red, dark grey and black after exposure to elevated  
159 temperatures of 300 °C, 581 °C, 804 °C and 1007 °C.

160

### 161 **2.3 Material tensile coupon tests**

162

163 Upon completion of the heating, soaking and cooling processes, tensile coupon tests were  
164 conducted by using a 50 kN servo-hydraulic tensile testing machine. A displacement-controlled  
165 loading scheme was used to drive the actuator of the testing machine; the loading rate was  
166 initially set to be equal to 0.05 mm/min up to the material nominal 0.2% proof stress (yield  
167 stress) at ambient temperature, after which a faster loading rate equal to 0.8 mm/min was  
168 employed for the post-yield stage, as recommended by Huang and Young [28]. The tensile  
169 coupon test setup is displayed in Fig. 4, where an extensometer is mounted onto the coupon to  
170 record the elongation between the 50 mm gauge length, and a pair of strain gauges are attached  
171 to the mid-height of the coupon to capture the tensile strains. The measured (post-fire and  
172 ambient temperature) stress–strain curves of the tensile coupons, extracted from CHS 73×3  
173 and CHS 89×3, are displayed in Figs 5(a) and 5(b), respectively, while the key measured  
174 material properties are listed in Table 2, including the Young’s modulus  $E$ , the 0.2% proof  
175 stress  $\sigma_{0.2}$ , the ultimate strength  $\sigma_u$ , the strain at the ultimate strength  $\varepsilon_u$ , and the coefficients



176 adopted in the component Ramberg–Osgood material model  $n$  and  $m$  [24, 29-34]. It was  
177 generally found that the material Young’s modulus and ultimate strength almost remain  
178 unchanged as the heating temperature increases, while the material 0.2% proof stress does not  
179 exhibit visible reductions for heating temperatures up to 600 °C, but experiences relatively  
180 rapid decreases at higher heating temperatures. A more detailed discussion on the material  
181 properties and stress–strain responses of grade EN 1.4301 austenitic stainless steel after  
182 exposure to elevated temperatures was presented by the authors in He et al. [24].

183

#### 184 ***2.4 Initial geometric imperfection measurements***

185

186 The flexural buckling behaviour and strengths of column members are sensitive to their initial  
187 global geometric imperfections. Thus, the initial global geometric imperfection of each  
188 stainless steel CHS column specimen was carefully measured prior to the pin-ended column  
189 tests. The experimental setup for initial global geometric imperfection measurements is shown  
190 in Fig. 6, where the column specimen is mounted on the work bench of a CNC router, and a  
191 LVDT is moved along the uppermost edge line of the specimen, with the readings respectively  
192 recorded near the two ends and at mid-height. The initial mid-height global geometric  
193 imperfection magnitude of the column specimen in the radial direction was given as the  
194 deviation from a linear reference line (i.e. a linear line connecting the data points at the two  
195 ends) to the measured data point at mid-height. The specimen was then rotated at an interval  
196 of 60 degrees, with the measurement procedures repeated, to derive the initial global geometric  
197 imperfection magnitudes in another five radial directions – see Fig. 6. The value of the initial  
198 global geometric imperfection of each column specimen  $\omega_g$  was defined as the maximum  
199 magnitude measured in all the six radial directions, as reported in Table 1.

200

## 201 **2.4 Pin-ended column tests**

202

203 Compression tests of pin-ended stainless steel CHS columns after exposure to fire were carried  
204 out, aimed at examining their post-fire flexural buckling behaviour and strengths, while  
205 comparative experiments were also conducted on the unheated reference column specimens.

206 All the column specimens were loaded in an Instron 5000 kN servo-hydraulic testing machine  
207 at a constant rate equal to 0.2 mm/min. Each end of the testing machine is equipped with a  
208 knife-edge device, offering pin-ended boundary condition to the specimens. The knife-edge  
209 device, as depicted in Fig. 7, consists of a pit plate with a semi-circular groove and a wedge  
210 plate containing a knife-edge wedge. Prior to testing, each column specimen was positioned  
211 between the top and bottom knife-edge devices, and oriented such that the radial direction  
212 leading to the maximum initial global geometric imperfection magnitude was perpendicular to  
213 the knife-edges. It is worth noting that the distance from the rotation centre of the knife-edge  
214 device to the end of the column specimen is equal to 55 mm; thus the effective member length  
215 of each column specimen is given as  $L_e=L+110$  mm, as listed in Table 1.

216

217 The column test rig is depicted in Fig. 7, including two LVDTs, positioned to the mid-height  
218 of the specimen, to measure the lateral deflections along the buckling direction, and a pair of  
219 strain gauges, stuck to the extreme fibres of the mid-height cross-section, to record the strains  
220 at these two positions along the longitudinal direction. The LVDT readings were adopted,  
221 together with the strain gauge values, to calculate the actual initial loading eccentricity about  
222 the buckling axis of each column specimen according to Eq. (1) [22, 35-38], where  $e_0$  is the  
223 calculated initial loading eccentricity,  $N$  is the applied compression load,  $\varepsilon_{\max}-\varepsilon_{\min}$  is the  
224 difference of the longitudinal strains measured from the two strain gauges,  $\Delta$  is the mid-height  
225 lateral deflection and  $I$  is the second moment of area of the circular hollow section; note that

226 Eq. (1) was derived based on an assumption that the structural behaviour was close to linear  
227 elastic, and it was thus recommended [22, 37, 38] that no more than 15% of the expected failure  
228 load be used in the calculation of  $e_0$ . If the calculated initial loading eccentricity, combined  
229 with the initial global geometric imperfection magnitude (i.e.  $\omega_g+e_0$ ), exceeded  $L_e/1000$  [1, 21,  
230 35], the position of the column specimen was carefully re-adjusted until the achievement of  
231  $(\omega_g+e_0)<L_e/1000$ .

$$e_0 = \frac{EI(\varepsilon_{\max} - \varepsilon_{\min})}{DN} - \Delta - \omega_g \quad (1)$$

233  
234 The experimental load–mid-height lateral deflection curves for the three series of stainless steel  
235 CHS column specimens are shown in Fig. 8. Table 3 summarised the key experimental results  
236 for the unheated and post-fire stainless steel CHS column specimens, including the combined  
237 initial global geometric imperfection magnitude and loading eccentricity ( $\omega_g+e_0$ ), the failure  
238 load  $N_u$  and the mid-height lateral deflection at the failure load  $\delta_u$ . In terms of the deformed  
239 failure modes, flexural buckling was generally observed for all the three specimen series; Fig.  
240 9 depicts the experimental failure modes for a typical specimen series D73-L9, including one  
241 unheated column specimen D73-L9-T30 and four post-fire column specimens D73-L9-T300,  
242 D73-L9-T600, D73-L9-T800 and D73-L9-T1000.

243

### 244 **3. Numerical modelling**

245

#### 246 **3.1 General**

247

248 In parallel with the experimental study, a numerical modelling programme was carried out by  
249 means of the finite element analysis package ABAQUS [39], and reported in this section. Finite  
250 element (FE) models were firstly developed and validated against the experimental results.

251 Parametric studies were then conducted using the validated FE models, to derive further  
252 numerical data over an extended range of cross-section sizes and member lengths.

253

### 254 ***3.2 Development of FE models***

255

256 Each stainless steel CHS column FE model was developed based on the measured cross-section  
257 geometric sizes and effective member lengths, as reported in Table 1. The shell element S4R  
258 [39] has been shown to be accurate and effective in previous numerical modelling of various  
259 types of stainless steel CHS structural components (e.g., columns [21, 40-42], beams [43] and  
260 beam-columns [13, 22, 23]), and was also adopted herein. The size of the employed S4R  
261 element was selected to be equal to  $0.1D$ , based on a prior mesh sensitivity study [24]; this  
262 element size was shown to be capable of offering both satisfactory computational efficiency  
263 and accuracy. With regard to the material modelling, the ambient temperature and post-fire  
264 material stress–strain curves measured from the tensile coupon tests were firstly converted into  
265 the true stress–true plastic strain curves, and afterwards assigned to the respective FE modes  
266 for stainless steel CHS columns at ambient temperature and after exposure to fire. For the ease  
267 of defining the boundary condition, all the nodes of each end section of the stainless steel CHS  
268 column FE model were coupled to a concentric reference point. The top reference point (at the  
269 loaded end) were restrained except for rotation about the buckling axis as well as longitudinal  
270 translation, whilst the bottom reference point was only allowed to rotate about the buckling  
271 axis, to replicate the same pin-ended boundary condition as that adopted in the tests. The initial  
272 local and global geometric imperfections were included into each stainless steel CHS column  
273 FE model in the form of the lowest elastic local and global buckling mode shapes [21, 22], as  
274 derived from the eigenvalue buckling analysis [39]. Two levels of initial local imperfection  
275 magnitudes, namely  $1/100$  and  $1/10$  of the wall thickness [13, 22], and three levels of initial

276 global imperfection values, including the measured total global imperfection value ( $\omega_g+e_0$ ) and  
277 1/1000 and 1/1500 of the member effective length, were adopted to factor the corresponding  
278 initial geometric imperfection patterns for each stainless steel CHS column FE model, resulting  
279 in a total of six combinations of initial local and global geometric imperfection magnitudes to  
280 be examined. The six initial local and global geometric imperfection magnitude combinations  
281 were employed to assess the influence of the initial geometric imperfection magnitudes on the  
282 ambient temperature and post-fire mechanical behaviour of stainless steel CHS columns and  
283 seek the most appropriate initial geometric imperfection magnitude combination to be  
284 employed in the parametric studies.

285

### 286 ***3.3 Validation of FE models***

287

288 Upon development of the stainless steel CHS column FE models, Riks analysis was performed  
289 to obtain the numerical failure loads, load–mid-height lateral deflection curves and failure  
290 modes, which were afterwards compared against their experimental counterparts, enabling the  
291 accuracy of the developed FE models to be assessed. Table 4 lists the test to numerical failure  
292 load ratios for the six combinations of initial local and global geometric imperfection  
293 magnitudes. It is evident that the experimental failure loads of the stainless steel CHS column  
294 specimens at ambient temperature and after exposure to fire were generally well captured for  
295 all the six examined initial geometric imperfection magnitude combinations. It is also worth  
296 noting that although the overall accuracy is deemed to be satisfied, there still exist discrepancies  
297 between the experimental and numerical failure loads for some specimens, with the main  
298 potential reason being that the actual initial geometric imperfections of the specimens and the  
299 idealised initial geometric imperfections (with elastic buckling mode shapes) of the FE modes  
300 are different. Moreover, the influence of the initial local geometric imperfection magnitudes

301 on the numerically predicted failure loads was much less significant than that of the initial  
302 global geometric imperfection magnitudes for the stainless steel CHS column specimens with  
303 non-slender cross-sections. The best agreement between the test and numerical failure loads  
304 was obtained when the measured total global imperfection magnitude ( $\omega_{g+e_0}$ ) and the initial  
305 local imperfection magnitude of  $t/100$  were adopted, while the combination, with the initial  
306 global imperfection magnitude of  $L_e/1000$  and initial local imperfection magnitude of  $t/100$   
307 also led to accurate numerical failure loads. The numerical load–mid-height lateral deflection  
308 curves for a typical specimen series D73-L6 are displayed in Fig. 10, together with their  
309 experimental counterparts, where the initial stiffnesses, general shapes and post-peak responses  
310 of the test load–deformation histories are found to be well replicated. Comparisons between  
311 the experimental and numerical failure modes for the typical specimen series D73-L9 are  
312 illustrated in Fig. 9, also indicating good agreement. Overall, the developed FE models are  
313 capable of accurately simulating the experimental flexural buckling responses of stainless steel  
314 CHS columns at ambient temperature and after exposure to fire, and thus deemed to be  
315 validated.

316

### 317 ***3.4 Parametric studies***

318

319 Having been validated in Section 3.3, the developed column FE models were subsequently  
320 used to conduct parametric studies, aimed at expanding the test data pool on stainless steel  
321 CHS columns after exposure to fire over an extended range of cross-section sizes and member  
322 lengths. Specifically, the outer cross-section diameter  $D$  was kept at 100 mm, with the wall  
323 thicknesses  $t$  varied between 0.86 mm and 4.65 mm; this leads to the  $D/t\epsilon^2$  ratios at ambient  
324 temperature ranging from 30 to 90, and covers all the three EC3 non-slender classes (i.e. Class  
325 1, 2 and 3) of circular hollow sections. The effective member lengths of the column FE models

326 were set to be varied between 500 mm (i.e. five times the outer cross-section diameter) and  
327 5500 mm (i.e. fifty-five times the outer cross-section diameter). The modelling procedures and  
328 techniques relevant to the development of stainless steel CHS column FE models, as presented  
329 in Section 3.2, were also employed in the present parametric studies, but with some  
330 supplementary information highlighted herein: (i) the measured material stress–strain curves  
331 of CHS 73×3 at ambient temperature and after exposure to four levels of elevated temperatures  
332 were used, and (ii) the initial local and global geometric imperfection magnitudes were  
333 respectively set to be equal to  $t/100$  and  $L_e/1000$ . In sum, a total of 385 numerical data on  
334 stainless steel CHS columns at ambient temperature and after exposed to fire were generated  
335 in the parametric studies.

336

## 337 **4. Evaluation of existing design standards**

338

### 339 ***4.1 General***

340

341 Due to the absence of established standards for the design of stainless steel structures after  
342 exposure to fire, the relevant design rules for stainless steel CHS columns at ambient  
343 temperature, as specified in the European code EN 1993-1-4 [25], American specification  
344 SEI/ASCE-8 [26] and Australian/New Zealand standard AS/NZS 4673 [27], were assessed  
345 herein for their applicability to stainless steel CHS columns after exposure to fire. In each of  
346 the following sub-sections, the codified design rules and formulations for stainless steel CHS  
347 columns at ambient temperature were firstly described. The unfactored flexural buckling  
348 strengths of the examined stainless steel CHS columns after exposure to fire were then  
349 calculated, based on the ambient temperature design formulations but with the post-fire  
350 material properties. Quantitative evaluation of the applicability of each design standard was

351 conducted by comparing the unfactored post-fire flexural buckling strengths  $N_u$  against the test  
 352 and numerical failure loads  $N_{u,pred}$ , with the mean ratios of  $N_u/N_{u,pred}$  and corresponding  
 353 coefficients of variation (COVs) summarised in Table 5.

354

#### 355 **4.2 European code EN 1993-1-4 (EC3)**

356

357 The existing European code EN 1993-1-4 [25] adopts buckling curves for the design of  
 358 stainless steel column members prone to global buckling (e.g., torsional, flexural and flexural-  
 359 torsional buckling) at ambient temperature. With regards to stainless steel CHS columns failing  
 360 by flexural buckling, the EC3 design strengths are given by Eq. (2),

$$361 \quad N_{u,EC3} = \chi A \sigma_{0.2} \quad (2)$$

362

363 where  $A$  is the cross-section area, respectively equal to the gross section area  $A_g$  and effective  
 364 section area  $A_{eff}$  for Class 1, 2 and 3 (non-slender) and Class 4 (slender) circular hollow sections,  
 365 and  $\chi$  is the reduction factor, as determined from the EC3 design buckling curve for stainless  
 366 steel CHS columns and given by Eq. (3),

$$367 \quad \chi = \frac{1}{\phi + \sqrt{\phi^2 - \bar{\lambda}^2}} \leq 1 \quad (3)$$

368

369 where  $\bar{\lambda}$  is the member non-dimensional slenderness and determined by Eq. (4), while  $\phi$  is a  
 370 buckling coefficient and calculated from Eq. (5), in which  $\bar{\lambda}_0$  and  $\alpha$  are respectively the  
 371 limiting slenderness and imperfection factor; for stainless steel CHS columns,  $\bar{\lambda}_0 = 0.4$  and  
 372  $\alpha = 0.49$ .

$$373 \quad \bar{\lambda} = \sqrt{\frac{A \sigma_{0.2} L_e^2}{\pi^2 EI}} \quad (4)$$



374 
$$\phi = 0.5[1 + \alpha(\bar{\lambda} - \bar{\lambda}_0) + \bar{\lambda}^2] \quad (5)$$

375

376 The EC3 design flexural buckling strengths of stainless steel CHS columns after exposure to  
377 fire were calculated herein using Eqs (2)–(5), but with the ambient temperature material  
378 properties replaced by the corresponding post-fire material properties, and then compared  
379 against the experimental and numerical failure loads. The mean ratios of  $N_u/N_{u,EC3}$  and the  
380 corresponding COVs for stainless steel CHS columns at ambient temperature and after  
381 exposure to various levels of elevated temperatures are reported in Table 5. The quantitative  
382 evaluation results revealed that the EC3 design flexural buckling curve generally yields  
383 inaccurate (unsafe and scattered) predictions of strengths for stainless steel CHS columns at  
384 ambient temperature and after exposed to fire. Fig. 11 depicts the normalised failure loads of  
385 stainless steel CHS columns at ambient temperature and after exposure to fire (by the cross-  
386 section yield loads  $A\sigma_{0.2}$ ) plotted against the member non-dimensional slendernesses, together  
387 with the EC3 design flexural buckling curve; note that the cross-section yield loads and  
388 member non-dimensional slendernesses for stainless steel CHS columns after exposure to fire  
389 were calculated, based on the corresponding post-fire material properties. It is also evident in  
390 Fig. 11 that (i) the normalised data points of stainless steel CHS columns at ambient  
391 temperature and after exposure to fire exhibit rather small differences and (ii) the EC3 design  
392 flexural buckling curve yields unsafe strength predictions for stainless steel CHS columns at  
393 ambient temperature and after exposure to fire. It is worth noting that the EC3 design flexural  
394 buckling curve for stainless steel cold-formed hollow section columns at ambient temperature  
395 was calibrated based mainly on the square hollow section (SHS) and rectangular hollow section  
396 (RHS) column buckling test results, due to the lack of CHS column test data at the time when  
397 the standard was produced. Cold-formed SHS and RHS benefit from material strength  
398 enhancements at the corner regions, and hence the EC3 design flexural buckling curve

399 calibrated based on the SHS and RHS column test data results in unsafe flexural buckling  
 400 strength predictions when applied to CHS columns.

401

#### 402 **4.2 American specification SEI/ASCE-8 (ASCE)**

403

404 The American specification SEI/ASCE-8 [26] specifies that the design axial strength of  
 405 stainless steel concentrically loaded compression member at ambient temperature is calculated  
 406 as the product of the design failure stress  $F_n$  and the effective cross-section area  $A_e$  determined  
 407 at the design failure stress, as given by Eq. (6). For doubly-symmetric tubular section columns  
 408 which are prone to flexural buckling but not susceptible to torsional and flexural-torsional  
 409 buckling, the design failure stress is equal to the corresponding design flexural buckling stress,  
 410 as derived from Eq. (7) using the tangent modulus method, in which  $E_T$  is the tangent modulus  
 411 of the material stress–strain curve at the design flexural buckling stress point; note that  
 412 cumbersome iterations are generally required in the determination of  $E_T$  and  $F_n$ . The effective  
 413 cross-section area  $A_e$  is given by Eq. (8), where  $K_c$  is the reduction factor and determined from  
 414 Eq. (9), in which  $C$  is the material proportional limit to 0.2% proof stress ratio and  $\lambda_c=3.048C$ .

$$415 \quad N_{u,ASCE} = F_n A_e \quad (6)$$

$$416 \quad F_n = \frac{\pi^2 E_T}{(kL/r)^2} \leq \sigma_{0.2} \quad (7)$$

$$417 \quad A_e = [1 - (1 - (\frac{E_T}{E})^2)(1 - K_c)]A \quad (8)$$

$$418 \quad K_c = \frac{(1 - C)(E / \sigma_{0.2})}{(8.93 - \lambda_c)(D/t)} + \frac{5.882C}{8.93 - \lambda_c} \leq 1 \quad (9)$$

419

420 The ASCE design axial strengths of stainless steel CHS columns after exposure to fire were  
 421 calculated, based on Eqs (6)–(9) and the post-fire material properties, and compared with the

422 corresponding test and numerical failure loads in Fig. 12, together with the ambient temperature  
423 data points. It was found that the SEI/ASCE-8 design flexural buckling strengths are generally  
424 unsafe for stainless steel CHS columns at ambient temperature and after exposure to fire; this  
425 can also be seen from the quantitative evaluation results given in Table 5. Note that the design  
426 stress in the tangent modulus method of SEI/ASCE-8 [26] is actually the Euler buckling stress  
427 derived with the use of tangent modulus. The design stress does not consider any detrimental  
428 effect from the initial global geometric imperfection, and is thus shown to overestimate the  
429 actual failure stress of stainless steel columns. Moreover, SEI/ASCE-8 [26] was shown to yield  
430 even more over-predicted though marginally more consistent flexural buckling strengths than  
431 EN 1993-1-4 [25].

432

#### 433 ***4.3 Australian/New Zealand standard AS/NZS 4673 (AS/NZS)***

434

435 Regarding the calculation of design axial strengths of stainless steel concentrically loaded  
436 compression members at ambient temperature, the Australian/New Zealand standard AS/NZS  
437 4673 [27] uses the same approach as that adopted in SEI/ASCE-8 [26], but also provides an  
438 alternative explicit approach [44]. Similarly to the EC3 design buckling curves, the AS/NZS  
439 explicit approach was also developed in accordance with the Perry-Robertson buckling formula.  
440 The design flexural buckling stress  $F_a$  is calculated from Eq. (10), in which  $\bar{\lambda}$  is the member  
441 non-dimensional slenderness and can be determined from Eq. (4), and  $\phi_a$  is the AS/NZS  
442 buckling coefficient and defined by Eq. (11), where  $\alpha$ ,  $\beta$ ,  $\lambda_0$  and  $\lambda_1$  are the parameters depending  
443 on the stainless steel grades; note that the values of  $\alpha$ ,  $\beta$ ,  $\lambda_0$  and  $\lambda_1$  are respectively taken as 1.59,  
444 0.28, 0.55 and 0.2 for the studied grade EN 1.4301 (i.e. Type 304) austenitic stainless steel.  
445 The AS/NZS design column flexural buckling strength is then calculated from Eq. (12) as the  
446 product of the design flexural buckling stress  $F_a$  and the effective cross-section area determined

447 at the design flexural buckling stress  $A_e$ ; note that  $A_e$  is also calculated from Eq. (8), but with a  
 448 different reduction factor given by Eq. (13).

$$449 \quad F_a = \frac{\sigma_{0.2}}{\phi_a + \sqrt{\phi_a^2 - \bar{\lambda}^2}} \leq \sigma_{0.2} \quad (10)$$

$$450 \quad \phi_a = 0.5 \{1 + \alpha[(\bar{\lambda} - \lambda_1)^\beta - \lambda_0] + \bar{\lambda}^2\} \quad (11)$$

$$451 \quad N_{u,AS/NZS} = F_a A_e \quad (12)$$

$$452 \quad K_c = \frac{(1-C)(E/\sigma_{0.2})}{(3.226 - \lambda_c)(D/t)} + \frac{0.178C}{3.226 - \lambda_c} \leq 1 \quad (13)$$

453  
 454 Evaluation of the applicability of the AS/NZS explicit approach to the design of stainless steel  
 455 CHS columns after exposure to fire was carried out herein through comparing the post-fire  
 456 flexural buckling strengths (calculated using Eqs (10)–(13) and the post-fire material properties)  
 457 with the experimental and numerical failure loads. Fig. 13 presents the  $N_u/N_{u,AS/NZS}$  ratios  
 458 plotted against the member non-dimensional slendernesses for both the ambient temperature  
 459 and post-fire data points. The design flexural buckling curve defined by the AS/NZS explicit  
 460 approach, as also depicted in Fig. 13, was shown to be capable of capturing the test and  
 461 numerical data points across the full range of member non-dimensional slenderness  $\bar{\lambda}$  and  
 462 resulting in safe, accurate and consistent flexural buckling strength predictions for stainless  
 463 steel CHS columns after exposure to fire as well as at ambient temperature. The mean test (or  
 464 numerical) to AS/NZS predicted failure load ratio  $N_u/N_{u,AS/NZS}$  and the corresponding COV, as  
 465 listed in Table 5, are equal to 1.119 and 0.103, respectively. Both the graphical and quantitative  
 466 evaluation results revealed that the AS/NZS 4673 explicit design approach for stainless steel  
 467 CHS columns at ambient temperature can be safely applied to their counterparts after exposure  
 468 to fire, with a high degree of design accuracy and consistency. It is worth noting that the  
 469 AS/NZS explicit approach was derived and calibrated based on a comprehensive set of finite

470 element data [44], including those for CHS columns, and thus found to yield more accurate and  
471 consistent flexural buckling strength predictions in comparison with the EC3 design buckling  
472 curve and ASCE tangent modulus method.

473

## 474 **5. Conclusions**

475

476 A thorough experimental and numerical investigation has been performed to examine the  
477 flexural buckling behaviour and residual strengths of stainless steel CHS columns after  
478 exposure to fire. The experimental study was performed on 12 austenitic stainless steel CHS  
479 column specimens after exposure to four levels of elevated temperatures and 3 unheated  
480 reference column specimens, and included material tensile coupon tests, initial geometric  
481 imperfection measurements and pin-ended column tests. In parallel with the experimental study,  
482 a numerical investigation was conducted. FE models were initially developed and validated  
483 against the experimental results, and then adopted to perform parametric studies, aimed at  
484 deriving further numerical data over an extended range of member lengths and cross-section  
485 sizes. Given that there have been no codified post-fire design rules for stainless steel CHS  
486 columns, the corresponding ambient temperature design rules, as specified in the current EN  
487 1993-1-4 [25], SEI/ASCE-8 [26] and AS/NZS 4673 [27], were assessed for their applicability  
488 to stainless steel CHS columns after exposure to fire, based on the experimental and numerical  
489 data. It was found that (i) the normalised data points of stainless steel CHS columns at ambient  
490 temperature and after exposure to fire (i.e. the failure loads normalised by the cross-section  
491 yield loads) exhibit rather small differences and (ii) the design buckling curve, as employed in  
492 EN 1993-1-4 [25], and the tangent modulus method, as adopted in SEI/ASCE-8 [26], yield  
493 generally unsafe and rather scattered predictions of flexural buckling strengths for stainless  
494 steel CHS columns after exposure to fire, and (iii) the explicit approach, as used in AS/NZS

495 4673 [27], was shown to lead to a high level of accuracy and consistency in the design of  
496 stainless steel CHS columns after exposure to fire, with safe, accurate and consistent post-fire  
497 flexural buckling strength predictions.

498

499

## 500 **References**

501

502 [1] Rasmussen KJR, Hancock GJ. Design of Cold - Formed Stainless Steel Tubular Members.

503 I: Columns. *Journal of Structural Engineering*. 1993;119:2349-67.

504 [2] Burgan BA, Baddoo NR, Gilsenan KA. Structural design of stainless steel members

505 comparison between Eurocode 3, Part 1.4 and test results. *Journal of Constructional Steel*

506 *Research*. 2000;54:51-73.

507 [3] Rasmussen KJR. Recent research on stainless steel tubular structures. *Journal of*

508 *Constructional Steel Research*. 2000;54:75-88.

509 [4] Young B, Hartono W. Compression tests of stainless steel tubular members. *J Struct Eng-*

510 *Asce*. 2002;128:754-61.

511 [5] Gardner L, Nethercot DA. Experiments on stainless steel hollow sections - Part 1: Material

512 and cross-sectional behaviour. *Journal of Constructional Steel Research*. 2004;60:1291-318.

513 [6] Bardi FC, Kyriakides S. Plastic buckling of circular tubes under axial compression - part I:

514 Experiments. *Int J Mech Sci*. 2006;48:830-41.

515 [7] Paquette JA, Kyriakides S. Plastic buckling of tubes under axial compression and internal

516 pressure. *Int J Mech Sci*. 2006;48:855-67.

517 [8] Lam D, Gardner L. Structural design of stainless steel concrete filled columns. *Journal of*

518 *Constructional Steel Research*. 2008;64:1275-82.

- 519 [9] Uy B, Tao Z, Han LH. Behaviour of short and slender concrete-filled stainless steel tubular  
520 columns. *Journal Of Constructional Steel Research*. 2011;67:360-78.
- 521 [10] Rasmussen KJR, Hancock GJ. Design of Cold-Formed Stainless-Steel Tubular  
522 Members .2. Beams. *J Struct Eng-Asce*. 1993;119:2368-86.
- 523 [11] Kiymaz G. Strength and stability criteria for thin-walled stainless steel circular hollow  
524 section members under bending. *Thin-Walled Structures*. 2005;43:1534-49.
- 525 [12] A. Talja, Test Report on Welded I and CHS Beams, Columns and Beam-Columns (Report  
526 to ECSC), VTT Building Technology, Finland, 1997.
- 527 [13] Zhao O, Gardner L, Young B. Structural performance of stainless steel circular hollow  
528 sections under combined axial load and bending – Part 1: Experiments and numerical  
529 modelling. *Thin-Walled Structures*. 2016;101:231-9.
- 530 [14] Zhao O, Gardner L, Young B. Structural performance of stainless steel circular hollow  
531 sections under combined axial load and bending – Part 2: Parametric studies and design. *Thin-*  
532 *Walled Structures*. 2016;101:240-8.
- 533 [15] Buchanan C, Gardner L, Liew A. The continuous strength method for the design of circular  
534 hollow sections. *Journal of Constructional Steel Research*. 2016;118:207-16.
- 535 [16] Afshan S, Gardner L. The continuous strength method for structural stainless steel design.  
536 *Thin-Walled Structures*. 2013;68:42-9.
- 537 [17] Zhao O, Afshan S, Gardner L. Structural response and continuous strength method design  
538 of slender stainless steel cross-sections. *Engineering Structures*. 2017;140:14-25.
- 539 [18] Ashraf M, Gardner L, Nethercot DA. Compression strength of stainless steel cross-  
540 sections. *Journal of Constructional Steel Research*. 2006;62:105-15.
- 541 [19] Ashraf M, Gardner L, Nethercot DA. Structural Stainless Steel Design: Resistance Based  
542 on Deformation Capacity. *Journal of Structural Engineering*. 2008;134:402-11.

- 543 [20] Gardner L. The continuous strength method for hot-rolled steel and steel-concrete  
544 composite design. *Proceedings of the Institution of Civil Engineers - Structures and Buildings*.  
545 2008;161:127-33.
- 546 [21] Buchanan C, Real E, Gardner L. Testing, simulation and design of cold-formed stainless  
547 steel CHS columns. *Thin-Walled Structures*. 2018;130:297-312.
- 548 [22] Zhao O, Gardner L, Young B. Testing and numerical modelling of austenitic stainless  
549 steel CHS beam–columns. *Engineering Structures*. 2016;111:263-74.
- 550 [23] Buchanan C, Zhao O, Real E, Gardner L. Cold-formed stainless steel CHS beam-columns  
551 – testing, simulation and design. *Engineering Structures*. (in press).
- 552 [24] He A, Liang Y, Zhao O. Experimental and numerical studies of austenitic stainless steel  
553 CHS stub columns after exposed to elevated temperatures. *Journal of Constructional Steel*  
554 *Research*. 2019;154:293-305.
- 555 [25] EN 1993-1-4:2006+A1:2015. Eurocode 3: design of steel structures – part 1. 4: general  
556 rules – supplementary rules for stainless steels, including amendment A1 (2015). Brussels:  
557 European Committee for Standardization (CEN); 2015.
- 558 [26] SEI/ASCE 8-02, Specification for the design of cold-formed stainless steel structural  
559 members, American Society of Civil Engineers (ASCE), Reston, 2002.
- 560 [27] AS/NZS 4673. Cold-formed stainless steel structures. Sydney: AS/NZS 4673:2001; 2001.
- 561 [28] Huang Y, Young B. The art of coupon tests. *Journal of Constructional Steel Research*,  
562 2014;96:159-175.
- 563 [29] Ramberg W, Osgood WR. Description of stress–strain curves by three parameters.  
564 Technical note no. 902. Washington DC: National Advisory Committee for Aeronautics; 1943.
- 565 [30] Hill HN. Determination of stress–strain relations from offset yield strength values.  
566 Technical note no. 927. Washington DC: National Advisory Committee for Aeronautics; 1944.



567 [31] Mirambell E, Real E. On the calculation of deflections in structural stainless steel beams:  
568 an experimental and numerical investigation. *Journal of Constructional Steel Research*.  
569 2000;54:109-33.

570 [32] Rasmussen KJR. Full-range stress–strain curves for stainless steel alloys. *Journal of*  
571 *Constructional Steel Research*. 2003;59:47-61.

572 [33] Arrayago I, Real E, Gardner L. Description of stress–strain curves for stainless steel alloys.  
573 *Materials & Design*. 2015;87:540-52.

574 [34] Tao Z, Wang X-Q, Hassan MK, Song T-Y, Xie L-A. Behaviour of three types of stainless  
575 steel after exposure to elevated temperatures. *Journal of Constructional Steel Research*. 2018.

576 [35] Gardner L, Bu Y, Theofanous M. Laser-welded stainless steel I-sections: Residual stress  
577 measurements and column buckling tests. *Engineering Structures*. 2016;127:536-48.

578 [36] Huang Y, Young B. Experimental investigation of cold-formed lean duplex stainless steel  
579 beam-columns. *Thin-Walled Structures*. 2014;76:105-17.

580 [37] Zhao O, Rossi B, Gardner L, Young B. Behaviour of structural stainless steel cross-  
581 sections under combined loading – Part I: Experimental study. *Engineering Structures*.  
582 2015;89:236-46.

583 [38] Zhao O, Gardner L, Young B. Experimental Study of Ferritic Stainless Steel Tubular  
584 Beam-Column Members Subjected to Unequal End Moments. *Journal of Structural*  
585 *Engineering*. 2016;142.

586 [39] ABAQUS. ABAQUS/standard user’s manual volumes I–III and ABAQUS CAE manual.  
587 Version 6.12. Pawtucket (USA): Hibbitt, Karlsson & Sorensen, Inc; 2012.

588 [40] Mohammed A, Afshan S. Numerical modelling and fire design of stainless steel hollow  
589 section columns. *Thin-Walled Structures*. 2019;144.

590 [41] Huang Y, Young B. Design of cold-formed stainless steel circular hollow section columns  
591 using direct strength method. *Engineering Structures*. 2018;163:177-83.

- 592 [42] Chan T-M, Zhao X-L, Young B. Cross-section classification for cold-formed and built-up  
593 high strength carbon and stainless steel tubes under compression. *Journal of Constructional*  
594 *Steel Research*. 2015;106:289-95.
- 595 [43] Bock M, Gardner L, Real E. Material and local buckling response of ferritic stainless steel  
596 sections. *Thin-Walled Structures*. 2015;89:131-41.
- 597 [44] Rasmussen KJ, Rondal J. Strength curves for metal columns. *Journal of Structural*  
598 *Engineering*, 1997;123(6):721-728.

**Table 1** Measured geometric properties of stainless steel CHS column specimens.

Specimen ID	$D$ (mm)	$t$ (mm)	$L$ (mm)	$L_e$ (mm)	$T_n$ (°C)	$T$ (°C)	$\omega_g$ (mm)
D73-L6-T30	72.72	2.79	438	548	30	30	0.04
D73-L6-T300	73.00	2.79	438	548	300	300	0.06
D73-L6-T600	72.97	2.80	438	548	600	581	0.03
D73-L6-T800	72.83	2.81	438	548	800	804	0.11
D73-L6-T1000	72.85	2.77	438	548	1000	1007	0.30
D73-L9-T30	72.73	2.79	658	768	30	30	0.09
D73-L9-T300	72.80	2.76	658	768	300	300	0.16
D73-L9-T600	72.70	2.78	658	768	600	581	0.12
D73-L9-T800	72.92	2.78	658	768	800	804	0.21
D73-L9-T1000	72.65	2.77	658	768	1000	1007	0.09
D89-L6-T30	89.87	2.78	534	644	30	30	0.14
D89-L6-T300	89.59	2.78	534	644	300	300	0.19
D89-L6-T600	89.11	2.76	534	644	600	581	0.13
D89-L6-T800	89.19	2.77	534	644	800	804	0.14
D89-L6-T1000	88.98	2.76	534	644	1000	1007	0.20

**Table 2** Summary of key measured material properties from tensile coupon tests.

Cross-section	$T$ (°C)	$E$ (GPa)	$\sigma_{0.2}$ (MPa)	$\sigma_u$ (MPa)	$\varepsilon_u$ (%)	$n$	$m$
CHS 73×3	30	194	303	735	47	3.4	2.4
	300	205	290	730	46	3.6	2.4
	581	201	287	702	50	7.8	2.4
	804	204	262	708	49	4.9	2.3
	1007	205	177	700	51	5.7	1.9
CHS 89×3	30	206	292	727	55	4.0	2.4
	300	193	288	723	55	7.4	2.4
	581	208	323	718	61	3.9	2.6
	804	205	284	707	57	6.6	2.4
	1007	203	215	672	62	5.7	2.1

**Table 3** Key experimental results of pin-ended stainless steel CHS columns at ambient temperature and after exposure to elevated temperatures.

Specimen ID	$T$ (°C)	$L$ (mm)	$L_e$ (mm)	$\omega_{g+e_0}$ (mm)	$N_u$ (kN)	$\delta_u$ (mm)
D73-L6-T30	30	438	548	0.25	185.6	3.43
D73-L6-T300	300	438	548	0.29	198.1	2.04
D73-L6-T600	581	438	548	0.27	193.1	2.09
D73-L6-T800	804	438	548	0.35	178.5	2.26
D73-L6-T1000	1007	438	548	0.53	111.1	4.08
D73-L9-T30	30	658	768	0.19	186.5	2.25
D73-L9-T300	300	658	768	0.25	187.0	2.15
D73-L9-T600	581	658	768	0.21	189.8	2.07
D73-L9-T800	804	658	768	0.30	170.9	1.55
D73-L9-T1000	1007	658	768	0.18	123.3	2.68
D89-L6-T30	30	534	644	0.34	235.2	2.97
D89-L6-T300	300	534	644	0.39	241.3	2.22
D89-L6-T600	581	534	644	0.32	251.7	3.07
D89-L6-T800	804	534	644	0.34	232.1	2.93
D89-L6-T1000	1007	534	644	0.40	165.7	5.88

**Table 4** Comparison of test failure loads with FE failure loads for various combinations of initial local and global geometric imperfection magnitudes.

Specimen	Test $N_u$ / FE $N_u$					
	$(\omega_{g+e_0})+t/100$	$L_e/1000+t/100$	$L_e/1500+t/100$	$(\omega_{g+e_0})+t/10$	$L_e/1000+t/10$	$L_e/1500+t/10$
D73-L6-T30	0.915	0.929	0.921	0.916	0.930	0.922
D73-L6-T300	1.015	1.028	1.019	1.014	1.027	1.019
D73-L6-T600	1.040	1.056	1.046	1.039	1.055	1.045
D73-L6-T800	1.022	1.032	1.023	1.023	1.033	1.024
D73-L6-T1000	0.945	0.946	0.936	0.944	0.945	0.935
D73-L9-T30	0.992	1.036	1.019	0.993	1.036	1.019
D73-L9-T300	1.056	1.096	1.078	1.056	1.096	1.078
D73-L9-T600	1.143	1.178	1.164	1.143	1.178	1.166
D73-L9-T800	1.089	1.121	1.105	1.089	1.121	1.105
D73-L9-T1000	1.175	1.215	1.197	1.174	1.214	1.197
D89-L6-T30	0.967	0.979	0.971	0.967	0.980	0.972
D89-L6-T300	1.040	1.053	1.045	1.041	1.053	1.045
D89-L6-T600	0.966	0.978	0.970	0.966	0.980	0.971
D89-L6-T800	1.018	1.031	1.022	1.019	1.032	1.023
D89-L6-T1000	0.950	0.961	0.952	0.950	0.962	0.952
Mean	1.022	1.043	1.031	1.022	1.043	1.032
COV	0.071	0.079	0.077	0.071	0.079	0.077

**Table 5** Comparisons of test and numerical failure loads with codified strength predictions.

Temperature	No. of test data	No. of numerical data	$N_u/N_{u,EC3}$		$N_u/N_{u,ASCE}$		$N_u/N_{u,AS/NZS}$	
			Mean	COV	Mean	COV	Mean	COV
$T=30\text{ }^\circ\text{C}$	3	77	0.961	0.156	0.977	0.147	1.097	0.100
$T=300\text{ }^\circ\text{C}$	3	77	0.954	0.162	0.978	0.148	1.091	0.097
$T=581\text{ }^\circ\text{C}$	3	77	1.046	0.123	0.949	0.151	1.199	0.076
$T=804\text{ }^\circ\text{C}$	3	77	0.977	0.150	0.962	0.153	1.121	0.082
$T=1007\text{ }^\circ\text{C}$	3	77	0.934	0.204	0.970	0.180	1.084	0.122
Total	15	385	0.975	0.163	0.967	0.156	1.119	0.103

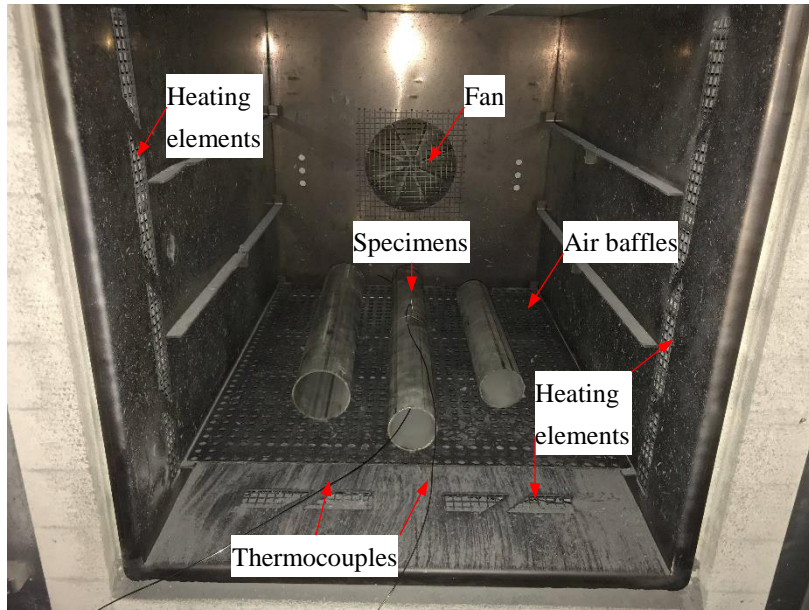


**Fig. 1.** Nabertherm forced convection furnace.

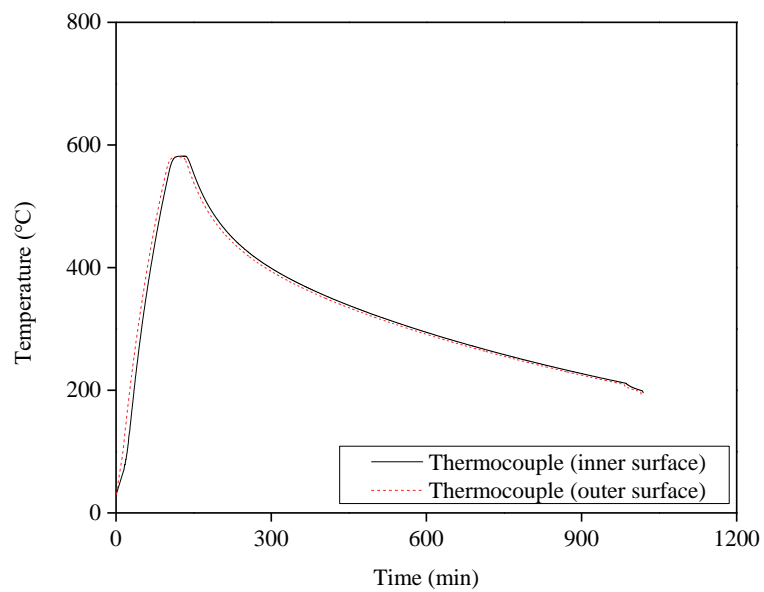


**Fig. 2.** Temperature–time curves for a typical group of specimens exposed to a target level of elevated temperature equal to 600 °C.

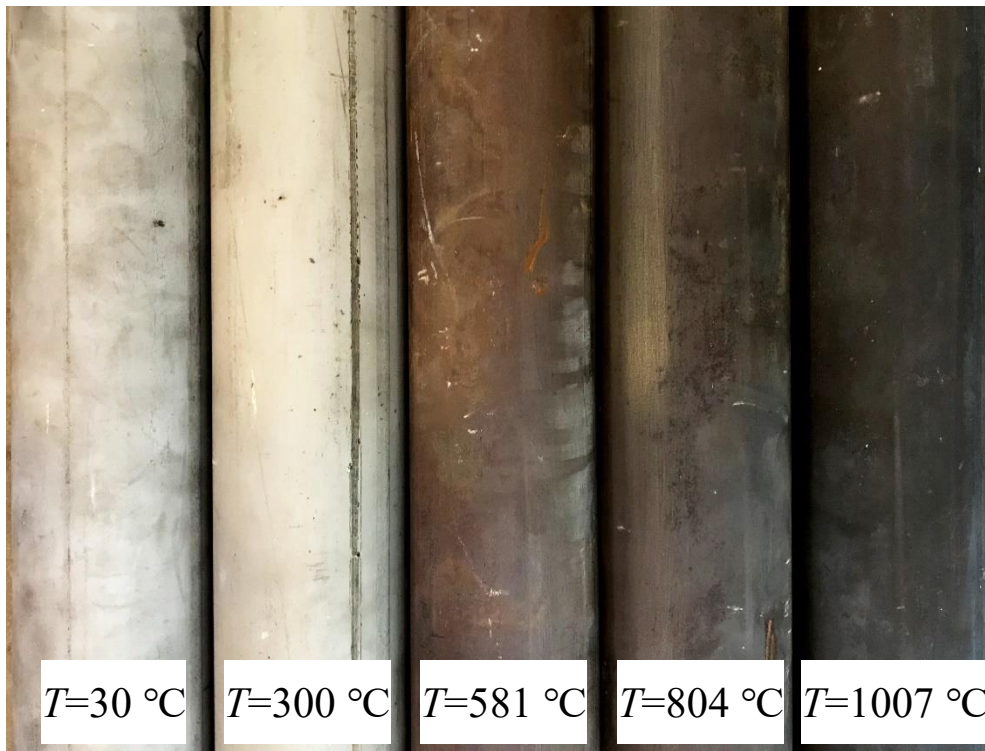
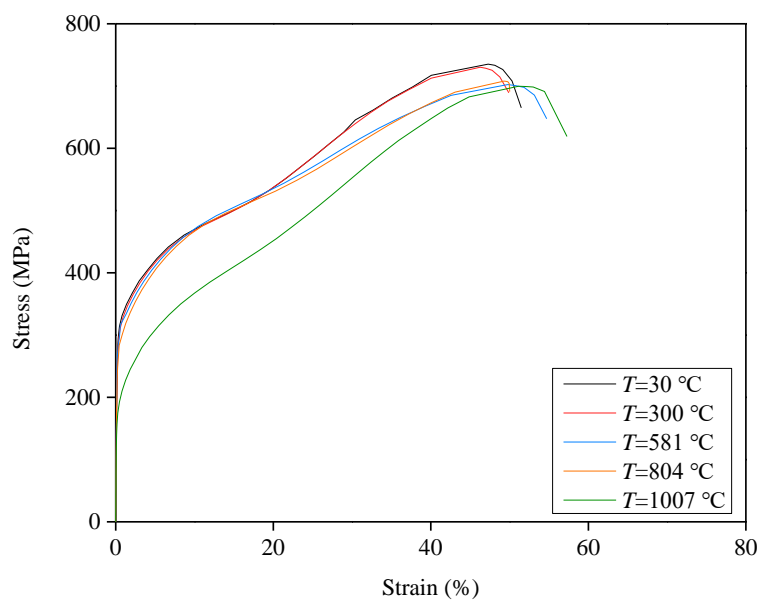


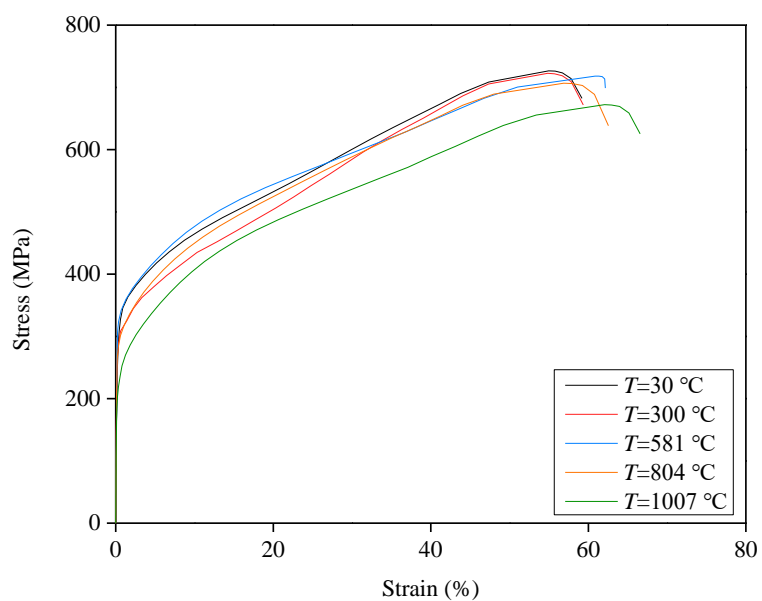
**Fig. 3.** Surface colours of austenitic stainless steel after exposure to various levels of elevated temperatures.



**Fig. 4.** Material tensile coupon test setup.



(a) CHS 73×3



(b) CHS 89×3

**Fig. 5.** Stress–strain curves of austenitic stainless steel at ambient temperature and after exposure to different levels of elevated temperatures.



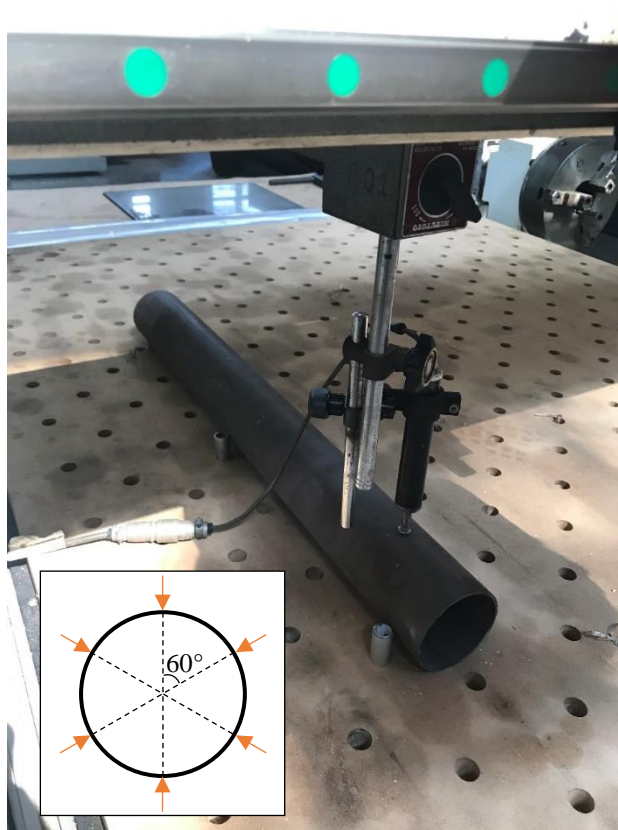
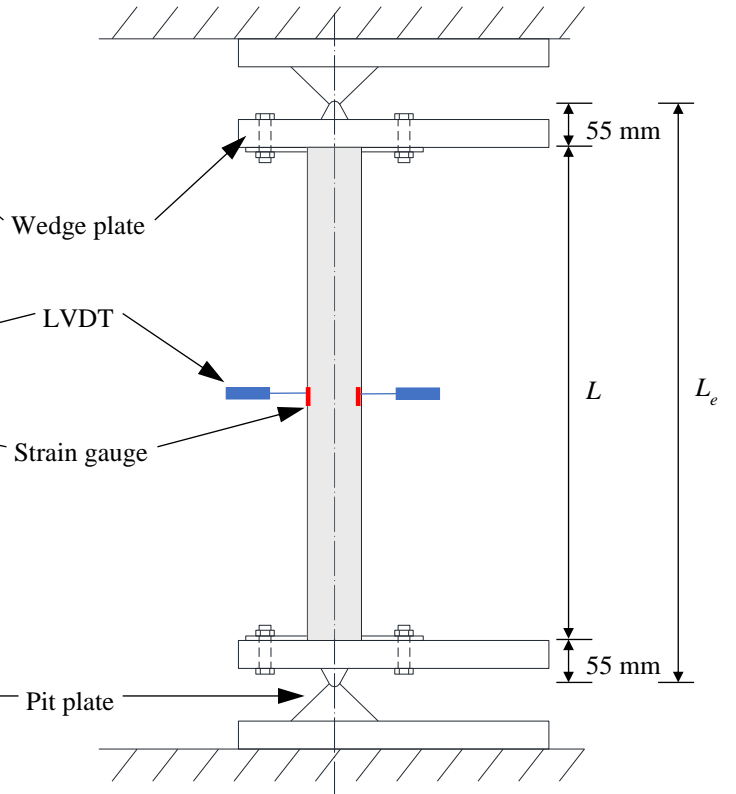


**Fig. 6.** Experimental setup for initial global geometric imperfection measurements.

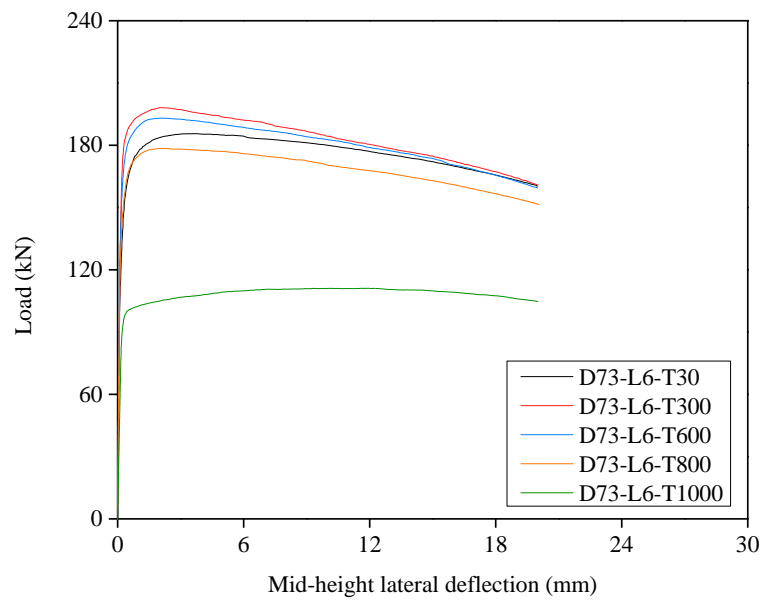


(a) Test setup

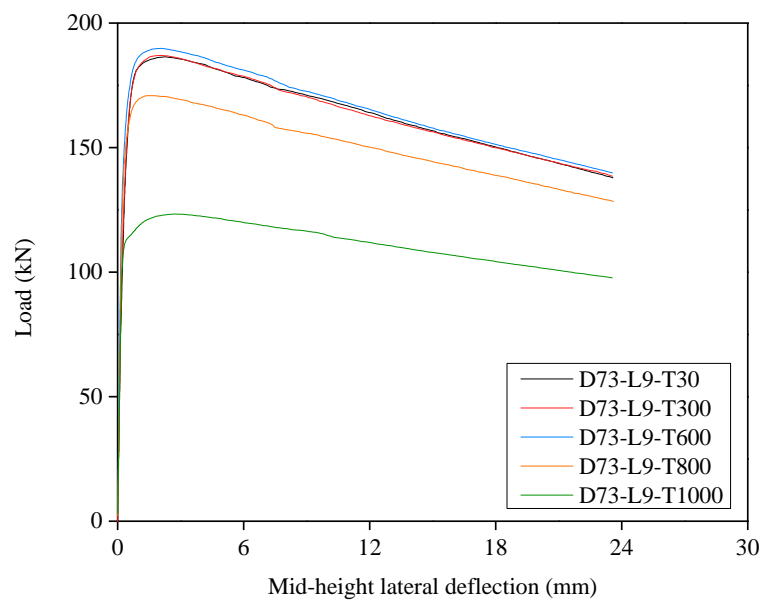


(b) Schematic diagram of the test setup

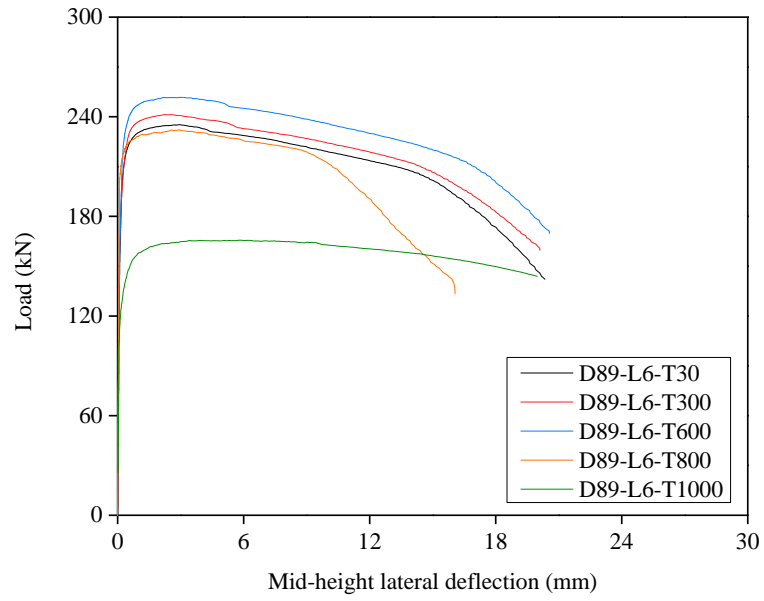
**Fig. 7.** Column test configuration.



(a) Specimen series D73-L6

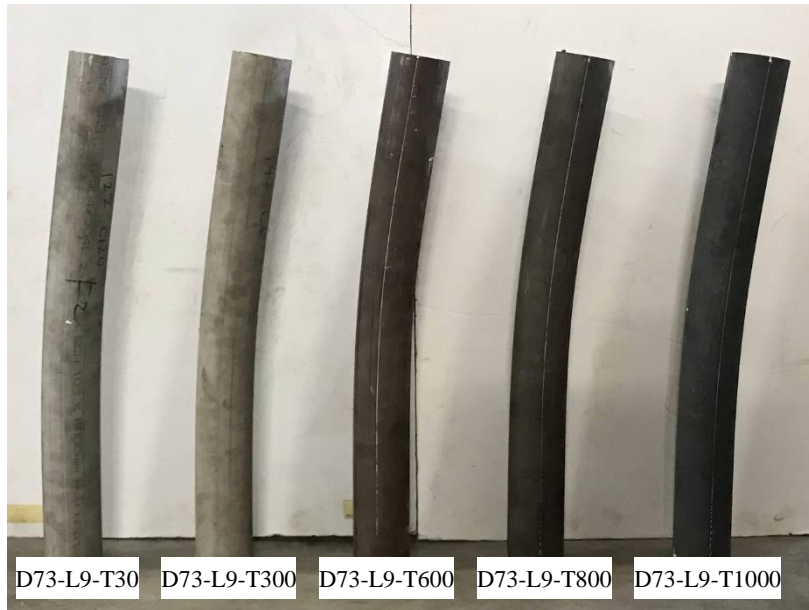


(b) Specimen series D73-L9

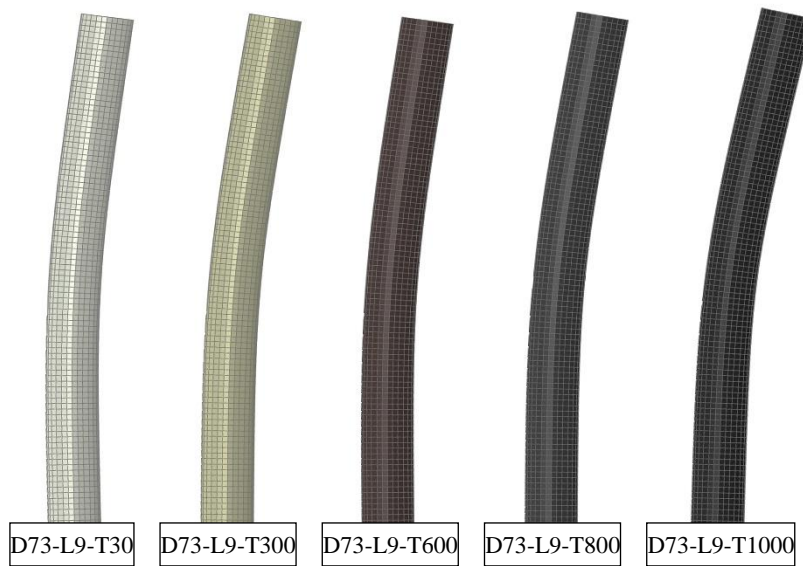


(c) Specimen series D89-L6

**Fig. 8.** Load–mid-height lateral deflection curves for pin-ended stainless steel CHS column specimens at room temperature and after exposure to elevated temperatures



(a) Experimental failure modes



(b) Numerical failure modes

**Fig. 9.** Experimental and numerical failure modes for a typical specimen series D73-L9.

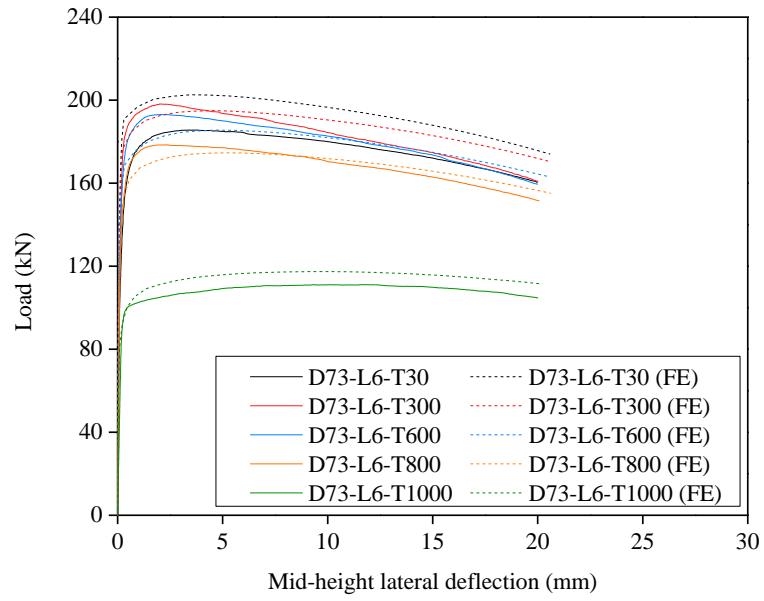


**Fig. 10.** Experimental and numerical load–mid-height lateral deflection curves for a typical specimen series D73-L6.

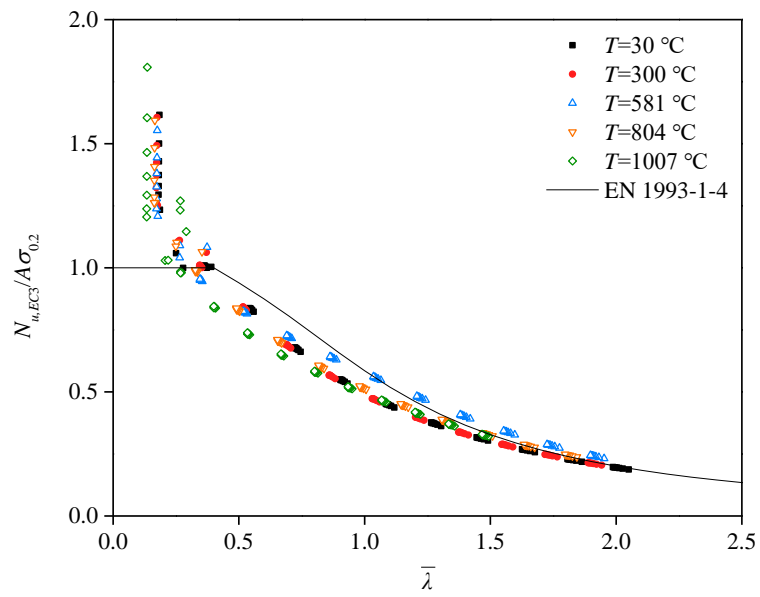


**Fig. 11.** Comparison of test and numerical failure loads with EC3 design flexural buckling curve.

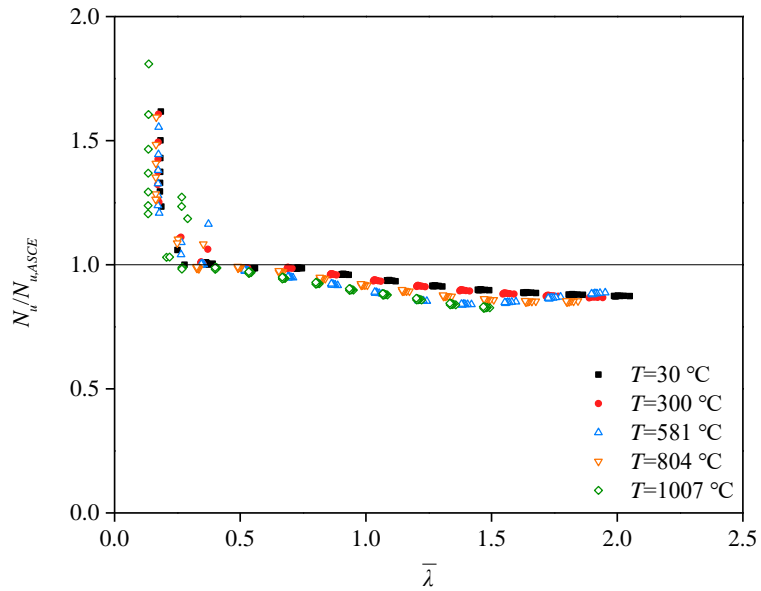


**Fig. 12.** Comparison of test and numerical failure loads with ASCE flexural buckling strength predictions.

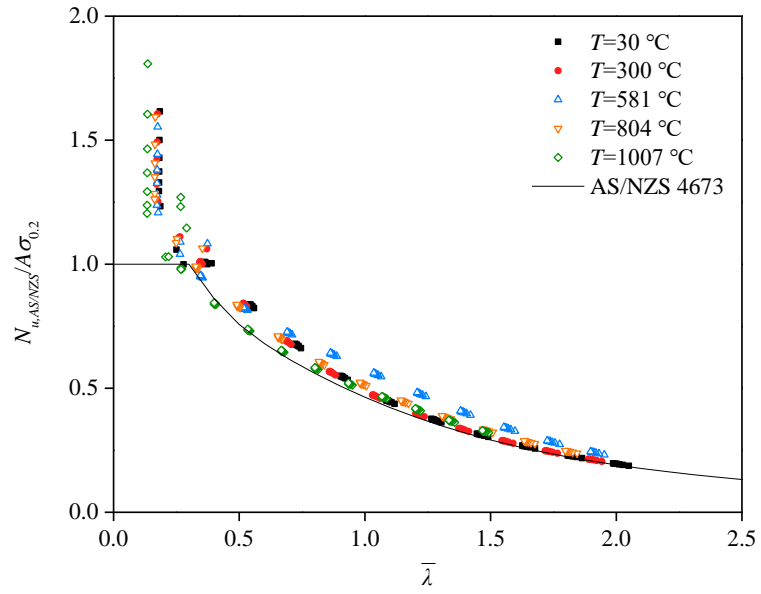


**Fig. 13.** Comparison of test and numerical failure loads with the AS/NZS design flexural buckling curve.